

Room temperature chiral magnetic skyrmion in ultrathin magnetic nanostructures

Olivier Boulle,^{1, 2, 3} Jan Vogel,^{4, 5} Hongxin Yang,^{1, 2, 3} Stefania Pizzini,^{4, 5} Dayane de Souza Chaves,^{4, 5} Andrea Locatelli,⁶ Tevfik Onur Menteş,⁶ Alessandro Sala,⁶ Liliana D. Buda-Prejbeanu,^{1, 2, 3} Olivier Klein,^{1, 2, 3} Mohamed Belmeguenai,⁷ Yves Roussigné,⁷ Andrey Stashkevich,⁷ Salim Mourad Chérif,⁷ Lucia Aballe,⁸ Michael Foerster,⁸ Maïrbek Chshiev,^{1, 2, 3} Stéphane Auffret,^{1, 2, 3} Ioan Mihai Miron,^{1, 2, 3} and Gilles Gaudin^{1, 2, 3}

¹ Univ. Grenoble Alpes, SPINTEC, F-38000 Grenoble, France

² CNRS, SPINTEC, F-38000 Grenoble, France

³ CEA, INAC-SPINTEC, F-38000 Grenoble, France

⁴ CNRS, Institut Néel, 25 avenue des Martyrs, B.P. 166, 38042 Grenoble Cedex 9, France

⁵ Univ. Grenoble Alpes, Institut Néel, 25 avenue des Martyrs, B.P. 166, 38042 Grenoble Cedex 9, France

⁶ Elettra-Sincrotrone, S.C.p.A, S.S 14 - km 163.5 in AREA Science Park 34149 Basovizza, Trieste, Italy

⁷ LSPM (CNRS-UPR 3407), Université Paris 13, Sorbonne Paris Cité,

99 avenue Jean-Baptiste Clément, 93430 Villetaneuse, France

⁸ ALBA Synchrotron Light Facility, Carretera BP 1413,

Km. 3.3, Cerdanyola del Valls, Barcelona 08290, Spain

Magnetic skyrmions are chiral spin structures with a whirling configuration. Their topological properties, nanometer size and the fact that they can be moved by small current densities have opened a new paradigm for the manipulation of magnetisation at the nanoscale. To date, chiral skyrmion structures have been experimentally demonstrated only in bulk materials and in epitaxial ultrathin films and under external magnetic field or at low temperature. Here, we report on the observation of stable skyrmions in sputtered ultrathin Pt/Co/MgO nanostructures, at room temperature and zero applied magnetic field. We use high lateral resolution X-ray magnetic circular dichroism microscopy to image their chiral Néel internal structure which we explain as due to the large strength of the Dzyaloshinskii-Moriya interaction as revealed by spin wave spectroscopy measurements. Our results are substantiated by micromagnetic simulations and numerical models, which allow the identification of the physical mechanisms governing the size and stability of the skyrmions.

The recent discovery of nanometer size whirling magnetic structures named magnetic skyrmions has opened a new path to manipulate magnetisation at the nanoscale [1–7]. A key feature of such magnetic nano-objects is their chiral and topologically non-trivial spin structure, i.e their magnetisation texture cannot be continuously transformed into the uniform magnetic state without causing a singularity [8]. For a surface C , this topological property is characterized by the skyrmion number $S = \frac{1}{4\pi} \int_C \mathbf{m} \cdot (\frac{\partial \mathbf{m}}{\partial x} \times \frac{\partial \mathbf{m}}{\partial y}) dx dy$ (\mathbf{m} is the unit magnetization vector). For a single skyrmion, $|S|$ is quantized and equal to 1 whereas $S = 0$ for the ferromagnetic state or any topologically trivial structure. The skyrmion chiral property is generally driven [2, 6] by an additional anti-symmetric term in the exchange energy, namely the Dzyaloshinskii-Moriya interaction (DMI), induced by the lack of structural inversion symmetry and the spin orbit coupling (SOC) [9, 10]. This additional energy term writes $E_{DM} = \mathbf{D} \cdot (\mathbf{S}_1 \times \mathbf{S}_2)$ where \mathbf{D} is the DMI characteristic vector and \mathbf{S}_1 and \mathbf{S}_2 are two neighbouring spins. Thus, the DMI tends to make the magnetisation rotate around \mathbf{D} . An additional important feature is that skyrmions can be manipulated by in-plane currents [11–14] which has led to novel concepts of non-volatile magnetic memories [7, 15] and logic devices [16] where skyrmions in nanotacks are the information carriers. The nm size of the skyrmion combined with the low current density needed to induce its motion [11, 13, 14] would lead to devices with unprecedented combination of high storage density, large data transfer rate and low power consumption [7, 15]. The topological ($|S| = 1$) and chiral properties of skyrmions are keys for such devices as they control the current induced skyrmion dynamics [7, 14, 17–20] and the interaction of skyrmions with other spin structures and the nanostructure edges [16, 19–23].

Although predicted at the end of the 80's [1], chiral skyrmion lattices and isolated skyrmions were observed only recently in B-20-type bulk or thin film chiral magnets [6] such as MnSi [3], $\text{Fe}_{1-x}\text{Co}_x\text{Si}$ [24], FeGe [25], $\text{Mn}_{1-x}\text{Fe}_x\text{Ge}$ [26] and in ultrathin magnetic films composed of Fe or Pd/Fe monolayers on Ir(111) [27–29]. In B-20 magnets, the DMI results from the non-centrosymmetric crystalline structure and Bloch-like skyrmions have been observed below room temperature [25] and in the presence of an external magnetic field [6]. In epitaxial heavy metal/ferromagnetic ultrathin films [27–29], the DMI arises from the breaking of inversion symmetry at the interfaces combined with the large spin-orbit coupling in the heavy metal [7], leading to skyrmions with a Néel-like structure [30, 31]. However, the observed skyrmions were stable only at low temperature [32] which prevents any use for applications. In addition, the ultrathin films were grown by molecular beam epitaxy which is not suitable for industrial production.

Recently, the attention has shifted to ultrathin ferromagnetic/heavy metal films deposited by sputtering [33]. This

class of materials combines several features which makes their use appealing for the study of skyrmion structures and their applications: i/ The magnetic parameters controlling the skyrmion stability and size, i.e the anisotropy, the DMI and the exchange [30, 34], can be easily tuned by playing with the nature and thickness of the materials composing the multilayers. ii/ They are characterized by a large DMI [35–38, 38, 41–44] which leads to chiral Néel domain walls (DWs) [45, 46]. iii/ Large current induced spin orbit torques are present [47, 48] which results in fast current induced DW motion [49, 50]. iv/ The deposition by sputtering is fast and spatially homogeneous and is compatible with standard spintronics devices such as magnetic tunnel junctions, which makes the industrial integration straightforward. Whereas several recent experimental works have studied magnetic bubbles in such materials [14, 18, 51, 52], and demonstrated their current induced motion [14, 52], the direct evidence of their chiral internal structure is still lacking. Here we report on the observation of stable chiral skyrmions in sputtered ultrathin Pt/Co(1 nm)/MgO nanostructures at room temperature and zero applied magnetic field. We used photoemission electron microscopy combined with X-ray magnetic circular dichroism (XMCD-PEEM) to demonstrate their chiral Néel internal structure. The XMCD-PEEM combines several advantages for the observation of magnetic nanostructures, such as skyrmions: firstly, a high lateral spatial resolution (down to 25 nm); secondly, the magnetic contrast is proportional to the projection of the local magnetisation along the X-ray beam direction. In our experiment, the X-ray beam impinges at a grazing angle of 16 degrees on the sample surface plane so that the contrast is approximately three times larger for the in-plane component of the magnetisation than for the out-of-plane one. This important feature allows the direct imaging of the internal in-plane spin structure of DWs or skyrmions.

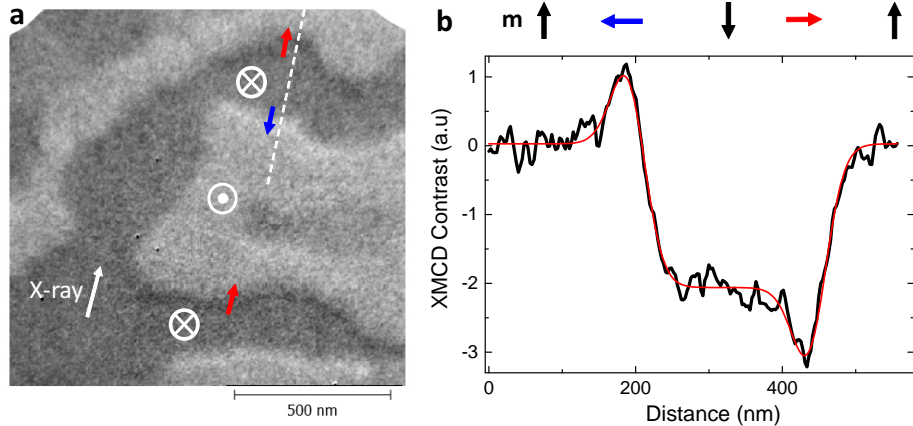


FIG. 1: Imaging of the chiral Néel structure of domain walls using XMCD-PEEM magnetic microscopy. (a) Magnetic image of a multidomain state in the continuous Pt/Co/MgO film. For DWs lying perpendicular to the X-ray beam direction, thin white and black lines can be seen, corresponding to the magnetisation being aligned antiparallel and parallel to the photon beam respectively. This demonstrates their chiral Néel structure. (b) Linescan of the magnetic contrast corresponding to the dotted white line in (a). To reduce the noise, the contrast has been averaged perpendicularly to the linescan over 60 nm. The red line is a fit assuming a chiral Néel DW structure convoluted by a Gaussian function to take into account the finite spatial resolution [53].

Observation of chiral Néel domain walls using XMCD-PEEM

All images shown here were acquired at room temperature and, unless otherwise stated, no external magnetic field was applied during the experiments. The PEEM observations were done in a virgin demagnetized state obtained after the sample nanofabrication and annealing. Complementary magnetisation measurements on unpatterned thin films show that the sample is magnetised perpendicularly to the film in the magnetic domains, which is due to a large interfacial uniaxial anisotropy. Figure 1(a) shows an XMCD-PEEM magnetic image of a multidomain state in the continuous film. Dark and bright grey regions correspond respectively to the magnetisation pointing down and up. Interestingly, we observe a sharp increase in the dichroic contrast for DWs perpendicular to the X-ray beam, with a strong dark contrast when going from an down to an up magnetized domain (along the beam direction) and a strong bright contrast when going from an up to a down magnetized domain. This can be seen more easily in the linescan of the magnetic contrast shown in Fig. 1(b), corresponding to the white dashed line in Fig. 1(a). A peak in

the contrast is observed at the up/down DW position while a dip is observed at the down/up DW position. Thus, the magnetisation in the up/down DW is aligned antiparallel to the in-plane direction of the X-ray beam whereas the magnetisation in the down/up DW is aligned parallel. We conclude that the DW magnetisation is perpendicular to the DW surface with an opposite magnetisation direction for the two DWs. This demonstrates that DWs in this material are chiral Néel DWs with a left-handed chirality. Note that for Bloch DWs, the magnetisation would be always perpendicular to the beam direction so that no peak or dip in the magnetic contrast should be observed. The linescan is well fitted assuming a chiral Néel DW structure, the finite resolution of the instrument being modeled by a Gaussian convolution (red curve, Fig. 1(b)). The fit leads to a DW width of 29.5 ± 4 nm ($\pi\sqrt{A/K_{eff}}$) [53].

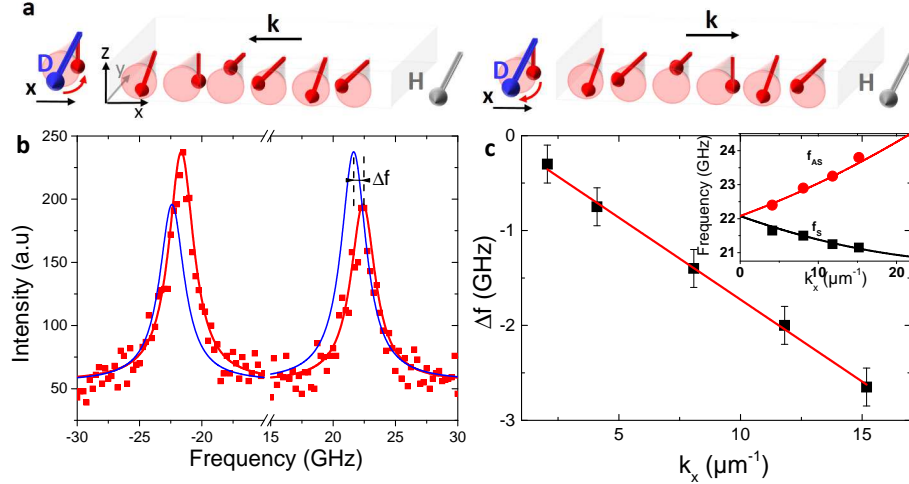


FIG. 2: **Brillouin Light Scattering spinwave spectroscopy.** (a) Principle of the measurement. At a given time t , when moving along x , the magnetisation rotates clockwise/counter-clockwise around the D vector for spin waves propagating along x (- x), which leads to different DM energy. (b) BLS spectra for an in-plane magnetic field $H=0.7$ T and $k_x = 4.1\mu\text{m}^{-1}$. The red squares are experimental data whereas the red lines are Lorentzian fits. The blue line is a Lorentzian fit of the experimental data inverted with respect to $f = 0$. (c) $\Delta f = f_S - f_{AS}$ as a function k_x for $H = 0.7$ T, where f_S and f_{AS} are respectively the Stokes and Anti-Stokes resonance frequency. Inset: f_S and f_{AS} as a function k_x .

Spin wave spectroscopy experiments and *ab-initio* calculations

The driving force of the DW and skyrmion chiral structure is the DMI. To further quantify its amplitude in our films, we measured the frequency shift of oppositely propagating spin waves using spin wave spectroscopy experiments [38–43]. The idea of the measurement is the following: When the magnetisation is pulled in the plane by an external magnetic field H_y , the D vector is oriented along y for spin waves propagating along the x axis (see Fig. 2(a)). Thus, at a given time t , when moving along the x axis, the magnetisation rotates anticlockwise around the D vector for spin waves with $k_x < 0$ and clockwise for $k_x > 0$. This leads to an energy shift for spin waves with opposite k_x vector due to the DMI and the corresponding frequency shift writes $\Delta f(k_x) = f(k_x) - f(-k_x) = 2\gamma k_x D / (\pi M_s)$. To measure Δf , we have carried out spin wave spectroscopy using the Brillouin Light Scattering technique in a backscattering geometry [43]. A spin wave spectrum is shown on Fig. 2(b) (red dots) for an in-plane magnetic field of 0.7 T and $k_x = 4.1\mu\text{m}^{-1}$. The Stokes (S) and Anti - Stokes(AS) peaks are observed, corresponding to $\pm k_x$. The blue line is a Lorentzian fit of the experimental data inverted with respect to $f = 0$, which shows that the Stokes peak has a frequency different to the Anti-Stokes peak, as is expected in the presence of DMI. The shift in frequency $\Delta f = f_S - f_{AS}$ scales linearly with k_x (Fig. 2(c)), which allows to extract a DM parameter $D = 2.05 \pm 0.3$ mJ/m². Note that the sign of Δf is consistent with the sign of D and the left handedness of the Néel DW we observe experimentally. As D is expected to be inversely proportional to the film thickness t [43], one can define a related interfacial DM parameter D_s such that $D = D_s/t$ and we find a value $D_s = 2.17 \pm 0.14$ pJ/m. To our knowledge, this value is the highest reported so far for a sputtered magnetic ultrathin film. To better understand this large value, we carried out *ab-initio* calculations of the DMI in Pt/Co(n ML)/vacuum and Pt/Co(n ML)/MgO multilayers [44, 53]. For n=5 ML of Co, equivalent to a total Co thickness of 1 nm, the *ab-initio* calculations predict $D = 2.3$ mJ/m² in relatively good agreement with experiments. Note that a lower value $D = 1.5$ mJ/m² is predicted for a Pt/Co[N]/vacuum structure,

which underlines the role played by the Co/oxide interface and in particular the large electric field due to the charge transfer between O and Co atoms.

Room-temperature skyrmion in a magnetic nanostructure

In continuous thin films, isolated magnetic bubbles [54] or chiral skyrmions [6] have been observed so far in the presence of a perpendicular magnetic field, which breaks the stripe domains or helical structure driven by the magnetostatic or DM energy. However, it is known that single magnetic bubbles can be stabilized without external magnetic fields using geometrical confinement in patterned nanostructures [55, 56]. Here we patterned different structures with various sizes and shapes (circular, square) in our Pt/Co/MgO thin films. Fig. 3(a) shows a circular magnetic domain stabilized in the middle of a 420 nm wide square dot, imaged at room temperature and no applied magnetic field. As observed in the multidomain structure, a sharp black/white contrast is observed at the DW position at the bottom/top of the central domain. This leads to a dip/peak in the dichroic contrast when doing a linescan along the domain diameter in the beam direction (see Fig. 3(b)). This indicates that the in-plane DW magnetisation is aligned parallel/antiparallel to the X-ray beam at the bottom/top of the reversed domain, i.e the DW surrounding the circular domain is a chiral Néel DW. This chiral border leads to a skyrmion number $|S| = 1$ for this structure. This demonstrates that the observed circular domain is a Néel like magnetic skyrmion. To extract the size of the skyrmion from the image, we assume that the magnetisation profile can be described by a 360° DW profile [29, 57, 58] : $\mathbf{m} = \sin \theta(r) \mathbf{u}_r + \cos \theta(r) \mathbf{u}_z$ with $\theta(r) = \theta_{DW}(r - d/2) + \theta_{DW}(r + d/2)$, where $\theta_{DW}(r) = 2 \arctan[\exp(r/\Delta)]$; d is the skyrmion diameter and Δ is the DW width. The unit vector \mathbf{u}_r is the polar unit vector. The blue curve (Fig. 3(b)) shows a fit of the experimental linescan assuming a Gaussian convoluted 360° DW and a good agreement is obtained with experimental data. From the fit, a skyrmion diameter $d = 130 \pm 2.5$ nm is extracted.

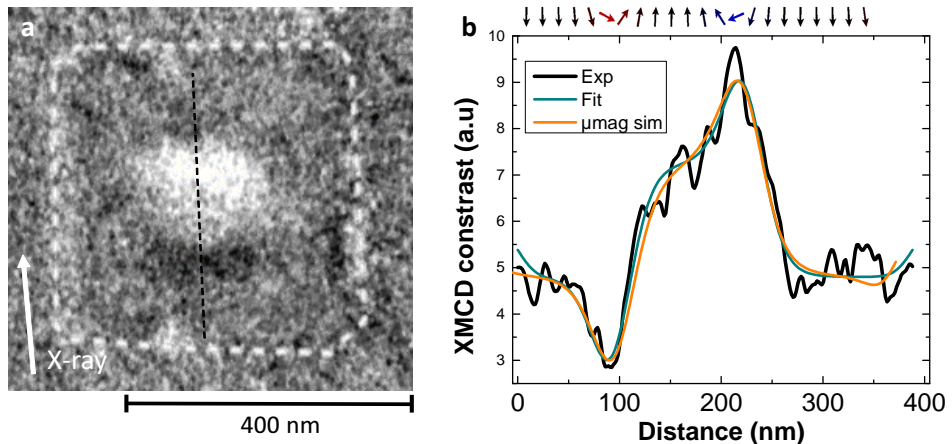


FIG. 3: **Magnetic skyrmion observed at room temperature and zero applied external magnetic field** (a) XMCD-PEEM image of a 420 nm square dot (indicated by the dotted line) and (b) linescan along the dotted black line (black line). The linescan has been averaged perpendicularly to the linescan over 30 nm. The blue line is a fit to the data using a Gaussian convoluted 360° DW profile [53]. The orange line is the contrast predicted by the micromagnetic simulations.

To better understand these experimental results, we carried out micromagnetic simulations using experimental values for the magnetocrystalline anisotropy constant K , the magnetic moment per surface area and the DMI interaction amplitude D . The exchange constant was used as a free parameter and the best agreement between experiments and micromagnetic simulations is obtained for $A = 27.5$ pJ/m, a value in line with previous measurements of A in ultra-thin magnetic multilayers [59]. Using these parameters, micromagnetic simulations predict a stable left-handed chiral skyrmion structure at zero external magnetic field (see Figure 4(a)) with a diameter of 128 nm and a DW width of 37 nm. From this magnetisation pattern, an experimental magnetic image can be simulated and a good agreement is obtained with the experimental results (see Fig. 4(b) and Fig. 3(b), orange curve for the simulated linescan). We show on Fig. 4(d) the same reconstructed experimental image assuming a Bloch DW structure. The image is rotated 90° with respect to the chiral Néel bubble structure and it is in clear disagreement with our experimental data. Finally, the simulations allow us to reconstruct the structure of the observed skyrmion. We show in Fig. 4(c) a linescan of the

in-plane (m_x) and out-of-plane (m_z) component of the magnetisation along the skyrmion diameter, as predicted by the micromagnetic simulation. The skyrmion diameter (~ 130 nm) being large compared to the DW width (37 nm), the magnetisation profile is close to two independent chiral Néel DWs, as can be seen on the m_z profile.

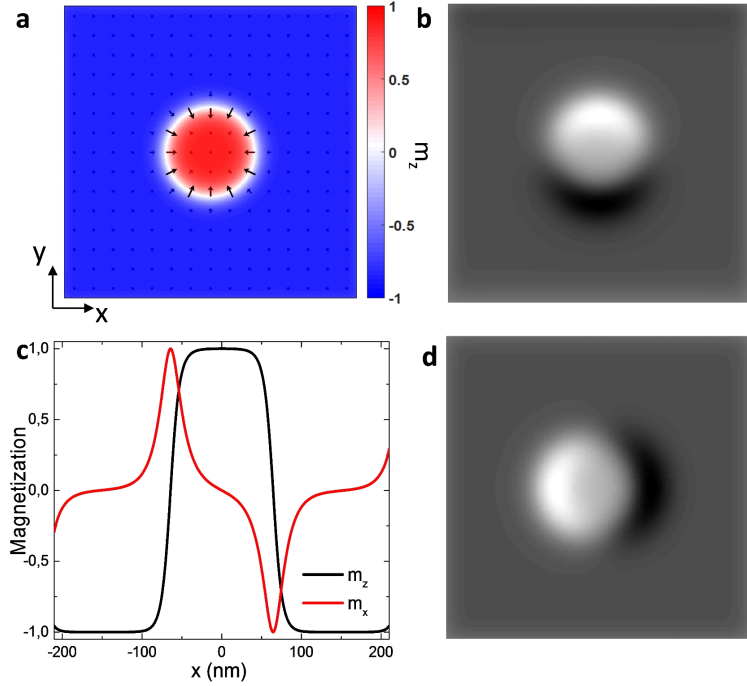


FIG. 4: **Micromagnetic simulations.** (a) Magnetisation distribution and (b) simulated magnetic contrast of the magnetic bubble in a 420 nm dot. (c) Magnetisation component m_x and m_z along the dotted white line in (a). (d) XMCD-PEEM contrast assuming a Bloch bubble structure. For the simulated magnetic contrast image, a spatial lateral resolution of 28 nm is assumed as obtained from the fit of the topological image of Fig. 3 [53].

Numerical calculations

The observation of stable skyrmions at zero external magnetic field raises the question of the physical mechanisms that govern the skyrmion stability and size in our experiments. To address this point, we consider a simple model where the magnetisation in the dot $\theta(r)$ is described by a circular 360° Néel DW profile. The free energy E in the circular dot-shaped nanostructure can be written as the sum of two terms [1, 30, 34, 60]: (1) the skyrmion energy $E_\sigma[\theta(r)]$ due to the exchange, anisotropy and internal DW stray field energies and (2) the energy due to the magnetostatic interactions between the domains E_{mag} . Assuming a radial symmetry, $E_\sigma[\theta(r)]$ can be written as [1, 30, 34, 60]:

$$E_\sigma[\theta(r)] = 2\pi t \int_0^R \left\{ A \left[\left(\frac{d\theta}{dr} \right)^2 + \frac{\sin^2 \theta}{r^2} \right] - D \left[\frac{d\theta}{dr} + \frac{\cos \theta \sin \theta}{r} \right] + (K_{eff} + E_{DW}^s) \sin^2 \theta \right\} r dr \quad (1)$$

where $K_{eff} = K - \mu_0 M_s^2 (1 - N_{DW})/2$ is the effective anisotropy [57, 61] (K is the magneto-crystalline anisotropy constant), t is the film thickness, R the dot radius. The demagnetizing energy due to the magnetic charges within the DWs E_{DW}^s is described by a constant demagnetizing factor N_{DW} such that $E_{DW}^s = N_{DW} \mu_0 M_s^2 / 2$. The energies E_σ and E_{mag} [62] can be evaluated as a function of the skyrmion diameter d assuming a 360° DW profile and a 420 nm diameter circular dot (the magnetic parameters correspond to the experiment of Fig 3, see methods). More physical insight is obtained from the effective forces $F_\sigma(d) = -\frac{\partial E_\sigma}{\partial d}$ and $F_{mag}(d) = -\frac{\partial E_{mag}}{\partial d}$ which are plotted in Fig. 5. A first interesting feature is that $F_\sigma(d)$ cancels out for $d \sim 20$ nm, which thus would be an equilibrium size for the skyrmion in the absence of the domain magnetostatic energy. This equilibrium is the result of a balance between the DW energy cost which is proportional to d and tends to decrease the skyrmion diameter and the curvature energy

cost due the exchange energy which scales as $1/d$ [34]. However, the magnetostatic force F_{mag} is large enough at low diameter to destabilize this balance and the final equilibrium position is obtained for a larger value of $d \sim 90$ nm, where the two forces are equal. This underlines that the magnetostatic energy plays an important role in the stability and size of the skyrmion at zero external magnetic field. We also carried out micromagnetic simulations for square nanostructures with larger lateral dimensions. We observed that for sides larger than $1.2 \mu\text{m}$, the skyrmion structure is not stable and a stripe domains structure appears [53]. This may explain why we did not observe any skyrmions but stripe domains for larger structures with $1 \mu\text{m}$ sides [53]. The confinement is thus an additional important feature for the skyrmion stability.

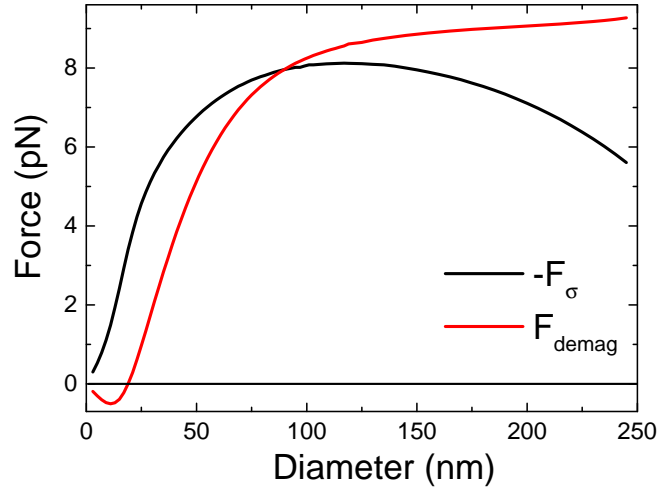


FIG. 5: **Forces acting on the DW as a function of the skyrmion diameter.** F_σ is the force due to the exchange and effective anisotropy (black curve), F_{mag} is the force due to the magnetostatic interaction between the domains (red curve).

It may seem surprising that the domain magnetostatic energy plays such an important role in the skyrmion stability given the very small thickness of the layer. Indeed, magnetostatic effects are expected to favor multidomain states only when the film thickness t is of the order or larger than the characteristic length $l_w = \sigma/(\mu_0 M_s^2)$, where σ is the DW surface energy. This criterion expresses the competition between the cost in the DW energy and the gain in the magnetostatic energy when creating a domain. The energy σ scales as $\sigma \sim 4\sqrt{AK_{eff}} - \pi D$ so that it is decreased in the presence of DMI. Thus, the criterion $l_w \sim t$ can be fulfilled even for very low thickness. In our experiments, we find that l_w is indeed of the order of the film thickness, $l_w \sim 1$ nm. This leads to the counterintuitive conclusion that the higher the DMI, the larger the role played by the magnetostatic interaction in the skyrmion stability. Note that this analysis holds for $\sigma > 0$, i.e $D < D_c$ where $D_c = 4\sqrt{AK_{eff}}/\pi$, which is the case in our sample where $D/D_c = 0.8$.

To conclude, we have observed stable magnetic skyrmions at room temperature in ultrathin Pt/Co/MgO films in the absence of applied external magnetic field. Using the high resolution XMCD-PEEM magnetic microscopy technique, we were able to demonstrate its internal left-handed chiral Néel structure, which can be explained by the large Dzyaloshinskii-Moriya interaction measured in this material. Micromagnetic simulations are in agreement with our experimental results and we show that the equilibrium skyrmion structure is the result of a balance between the DW energy modulated by the DMI and the magnetostatic interaction in the patterned structure. This balance is very sensitive to the different magnetic parameters that are D , K , A and the total magnetic moment. The lateral confinement also plays an important role since it leads to a modulation of the magnetostatic energy. Hence, the size and stability of magnetic skyrmions can be finely tuned by playing with these different parameters. This will be a key for the design of future devices based on the manipulation of magnetic skyrmions.

[1] Bogdanov, A. N. & Yablonskii, D. Thermodynamically stable "vortices" in magnetically ordered crystals. the mixed state of magnets. *J. Exp. Theor. Phys.* 178 (1989).

[2] Rößler, U. K., Bogdanov, A. N. & Pfleiderer, C. Spontaneous skyrmion ground states in magnetic metals. *Nature* **442**, 797–801 (2006).

[3] Mühlbauer, S. *et al.* Skyrmion lattice in a chiral magnet. *Science* **323**, 915–919 (2009).

[4] Pappas, C. *et al.* Chiral paramagnetic skyrmion-like phase in MnSi. *Phys. Rev. Lett.* **102**, 197202 (2009).

[5] Yu, H., Granville, S., Yu, D. P. & Ansermet, J.-P. Evidence for thermal spin-transfer torque. *Phys. Rev. Lett.* **104**, 146601 (2010).

[6] Nagaosa, N. & Tokura, Y. Topological properties and dynamics of magnetic skyrmions. *Nat Nano* **8**, 899–911 (2013).

[7] Fert, A., Cros, V. & Sampaio, J. Skyrmions on the track. *Nat Nano* **8**, 152–156 (2013).

[8] Braun, H.-B. Topological effects in nanomagnetism: from superparamagnetism to chiral quantum solitons. *Advances in Physics* **61**, 1–116 (2012).

[9] Moriya, T. Anisotropic superexchange interaction and weak Ferromagnetism. *Phys. Rev.* **120**, 91–98 (1960).

[10] Dzyaloshinskii, I. E. *Sov. Phys. JETP* **5**, 1259 (1957).

[11] Jonietz, F. *et al.* Spin transfer torques in MnSi at ultralow current densities. *Science* **330**, 1648–1651 (2010).

[12] Schulz, T. *et al.* Emergent electrodynamics of skyrmions in a chiral magnet. *Nat Phys* **8**, 301–304 (2012).

[13] Yu, X. Z. *et al.* Skyrmion flow near room temperature in an ultralow current density. *Nat Commun* **3**, 988 (2012).

[14] Jiang, W. *et al.* Blowing magnetic skyrmion bubbles. *Science* **349**, 283 (2015).

[15] Koshiba, W. *et al.* Memory functions of magnetic skyrmions. *Japanese Journal of Applied Physics* **54**, 053001 (2015).

[16] Zhang, X., Ezawa, M. & Zhou, Y. Magnetic skyrmion logic gates: conversion, duplication and merging of skyrmions. *Sci. Rep.* **5**, 9400 (2015).

[17] Moutafis, C., Komineas, S. & Bland, J. A. C. Dynamics and switching processes for magnetic bubbles in nanoelements. *Phys. Rev. B* **79**, 224429 (2009).

[18] Büttner, F. *et al.* Dynamics and inertia of skyrmionic spin structures. *Nat Phys* **11**, 225–228 (2015).

[19] Sampaio, J., Cros, V., Rohart, S., Thiaville, A. & Fert, A. Nucleation, stability and current-induced motion of isolated magnetic skyrmions in nanostructures. *Nat. Nanotechnol.* **8**, 839–844 (2013).

[20] Tomasello, R. *et al.* A strategy for the design of skyrmion racetrack memories. *Sci. Rep.* **4**, 6784 (2014).

[21] Iwasaki, J., Mochizuki, M. & Nagaosa, N. Current-induced skyrmion dynamics in constricted geometries. *Nat Nano* **8**, 742–747 (2013).

[22] Zhou, Y. & Ezawa, M. A reversible conversion between a skyrmion and a domain-wall pair in a junction geometry. *Nat Commun* **5**, 4652 (2014).

[23] Zhang, X. *et al.* Skyrmion-skyrmion and skyrmion-edge repulsions in skyrmion-based racetrack memory. *Sci. Rep.* **5**, 7643 (2015).

[24] Yu, X. Z. *et al.* Real-space observation of a two-dimensional skyrmion crystal. *Nature* **465**, 901–904 (2010).

[25] Yu, X. Z. *et al.* Near room-temperature formation of a skyrmion crystal in thin-films of the helimagnet FeGe. *Nat Mater* **10**, 106–109 (2011).

[26] Shibata, K. *et al.* Towards control of the size and helicity of skyrmions in helimagnetic alloys by spin-orbit coupling. *Nature Nanotechnology* **8**, 723–728 (2013).

[27] Heinze, S. *et al.* Spontaneous atomic-scale magnetic skyrmion lattice in two dimensions. *Nat Phys* **7**, 713–718 (2011).

[28] Romming, N. *et al.* Writing and deleting single magnetic skyrmions. *Science* **341**, 636–639 (2013).

[29] Romming, N., Kubetzka, A., Hanneken, C., von Bergmann, K. & Wiesendanger, R. Field-dependent size and shape of single magnetic skyrmions. *Phys. Rev. Lett.* **114**, 177203 (2015).

[30] Bogdanov, A. & Hubert, A. Thermodynamically stable magnetic vortex states in magnetic crystals. *Journal of Magnetism and Magnetic Materials* **138**, 255–269 (1994).

[31] Bogdanov, A. & Hubert, A. The stability of vortex-like structures in uniaxial ferromagnets. *Journal of Magnetism and Magnetic Materials* **195**, 182–192 (1999).

[32] Sonntag, A., Hermenau, J., Krause, S. & Wiesendanger, R. Thermal stability of an interface-stabilized skyrmion lattice. *Phys. Rev. Lett.* **113**, 077202 (2014).

[33] Monso, S. *et al.* Crossover from in-plane to perpendicular anisotropy in Pt/CoFe/AlOx sandwiches as a function of Al oxidation: A very accurate control of the oxidation of tunnel barriers. *Appl. Phys. Lett.* **80**, 4157–4159 (2002).

[34] Rohart, S. & Thiaville, A. Skyrmion confinement in ultrathin film nanostructures in the presence of Dzyaloshinskii–Moriya interaction. *Phys. Rev. B* **88**, 184422 (2013).

[35] Freimuth, F., Blügel, S. & Mokrousov, Y. Berry phase theory of Dzyaloshinskii–Moriya interaction and spin–orbit torques. *J. Phys.: Condens. Matter* **26**, 104202 (2014).

[36] Emori, S. *et al.* Spin hall torque magnetometry of Dzyaloshinskii domain walls. *Phys. Rev. B* **90**, 184427 (2014).

[37] Pizzini, S. *et al.* Chirality-induced asymmetric magnetic nucleation in Pt/Co/AlOx ultrathin microstructures. *Phys. Rev. Lett.* **113**, 047203 (2014).

[38] Di, K. *et al.* Asymmetric spin-wave dispersion due to Dzyaloshinskii–Moriya interaction in an ultrathin Pt/CoFeB film. *Appl. Phys. Lett.* **106**, 052403 (2015).

[39] Cortés Ortuño, D. & Landeros, P. Influence of the Dzyaloshinskii–Moriya interaction on the spin-wave spectra of thin films. *J. Phys.: Condens. Matter* **25**, 156001 (2013).

[40] Moon, J.-H. *et al.* Spin-wave propagation in the presence of interfacial Dzyaloshinskii–Moriya interaction. *Phys. Rev. B* **88**, 184404 (2013).

[41] Nembach, H. T., Shaw, J. M., Weiler, M., Jué, E. & Silva, T. J. Linear relation between Heisenberg exchange and interfacial Dzyaloshinskii–Moriya interaction in metal films. *Nature Physics* **11**, 825–829 (2015).

[42] Stashkevich, A. A. *et al.* Experimental study of spin-wave dispersion in Py/Pt film structures in the presence of an interface

Dzyaloshinskii-Moriya interaction. *Physical Review B* **91**, 214409 (2015).

[43] Belmeguenai, M. *et al.* Interfacial Dzyaloshinskii-Moriya interaction in perpendicularly magnetized Pt/Co/AlO_x ultrathin films measured by Brillouin light spectroscopy. *Phys. Rev. B* **91**, 180405 (2015).

[44] Yang, H., Thiaville, A., Rohart, S., Fert, A. & Chshiev, M. Anatomy of Dzyaloshinskii-Moriya interaction at Co/Pt interfaces. *Phys. Rev. Lett.* **115**, 267210 (2015).

[45] Chen, G. *et al.* Novel chiral magnetic domain wall structure in Fe/ Ni/Cu(001) films. *Phys. Rev. Lett.* **110**, 177204 (2013).

[46] Tetienne, J.-P. *et al.* The nature of domain walls in ultrathin ferromagnets revealed by scanning nanomagnetometry. *Nat Commun* **6**, 6733 (2015).

[47] Miron, I. M. *et al.* Perpendicular switching of a single ferromagnetic layer induced by in-plane current injection. *Nature* **476**, 189–193 (2011).

[48] Garello, K. *et al.* Symmetry and magnitude of spin-orbit torques in ferromagnetic heterostructures. *Nat Nano* **8**, 587–593 (2013).

[49] Miron, I. M. *et al.* Fast current-induced domain-wall motion controlled by the Rashba effect. *Nat Mater* **10**, 419–423 (2011).

[50] Thiaville, A., Rohart, S., Jué, É., Cros, V. & Fert, A. Dynamics of Dzyaloshinskii domain walls in ultrathin magnetic films. *Europhys. Lett.* **100**, 57002 (2012).

[51] Moreau-Luchaire, C. *et al.* Skyrmions at room temperature : From magnetic thin films to magnetic multilayers. *ArXiv150207853 Cond-Mat* (2015).

[52] Woo, S. *et al.* Observation of room temperature magnetic skyrmions and their current-driven dynamics in ultrathin Co films. *ArXiv150207376 Cond-Mat* (2015).

[53] See Supplementary Information.

[54] Slonczewski, J., Malozemoff & P., A. *Magnetic domain walls in bubble materials* (Academic Press, New-York, 1979).

[55] Hehn, M. *et al.* Nanoscale magnetic domains in mesoscopic magnets. *Science* **272**, 1782–1785 (1996).

[56] Moutafis, C. *et al.* Magnetic bubbles in FePt nanodots with perpendicular anisotropy. *Physical Review B* **76**, 104426 (2007).

[57] Braun, H.-B. Fluctuations and instabilities of ferromagnetic domain-wall pairs in an external magnetic field. *Phys. Rev. B* **50**, 16485–16500 (1994).

[58] Kubetzka, A., Pietzsch, O., Bode, M. & Wiesendanger, R. Spin-polarized scanning tunneling microscopy study of 360° walls in an external magnetic field. *Phys. Rev. B* **67**, 020401 (2003).

[59] Metaxas, P. J. *et al.* Creep and flow regimes of magnetic domain-wall motion in ultrathin Pt/Co/Pt films with perpendicular anisotropy. *Phys. Rev. Lett.* **99**, 217208 (2007).

[60] Kiselev, N. S., Bogdanov, A. N., Schäfer, R. & Rößler, U. K. Chiral skyrmions in thin magnetic films: new objects for magnetic storage technologies? *J. Phys. D: Appl. Phys.* **44**, 392001 (2011).

[61] Braun, H.-B. Nucleation in ferromagnetic nanowires—magnetostatics and topology. *Journal of Applied Physics* **85**, 6172–6174 (1999).

[62] Guslienko, K. Skyrmion state stability in magnetic nanodots with perpendicular anisotropy. *IEEE Magn. Lett.* **6**, 1–4 (2015).

[63] Chen, K. & Zhang, S. Spin pumping in the presence of spin-orbit Coupling. *Phys. Rev. Lett.* **114**, 126602 (2015).

[64] Mentes, T. O., Zamborlini, G., Sala, A. & Locatelli, A. *Beilstein J. Nanotechnol.* **5**, 1873886 (2014).

[65] Aballe, L., Foerster, M., Pellegrin, E., Nicolas, J. & Ferrer, S. The alba spectroscopic leem-peem experimental station: layout and performance. *Journal of Synchrotron Radiation* (2015).

[66] Buda, L. D., Prejbeanu, I. L., Ebels, U. & Ounadjela, K. *Comput. Mater. Sci.* **24**, 181 (2002).

[67] Vansteenkiste, A. & Van de Wiele, B. MuMax: A new high-performance micromagnetic simulation tool. *Journal of Magnetism and Magnetic Materials* **323**, 2585–2591 (2011).

[68] Donahue, M. J. & Porter, D. G. OOMMF user's guide, version 1.0 M.J. Donahue and D.G. MD. Tech. Rep., National Institute of Standards and Technology, Gaithersburg (1999).

Methods

Sample preparation and magnetic microscopy experiment The Ta(3)/Pt(3)/Co(0.5-1)/MgO_x/Ta(1) (thickness in nm) film was deposited by magnetron sputtering on a 100 mm high resistivity Si wafer, then annealed for 1.5 h at 250° C under vacuum and under an in-plane magnetic field of $\mu_0 H = 240$ mT. The Co layer was deposited as a wedge using a rotating cover during the deposition. The nominal thickness at the position of observation is $t = 0.98$ nm. The samples were patterned in different shapes (circle, square) and sizes using standard nanofabrication techniques. The XMCD-PEEM magnetic microscopy experiments were carried out with the SPELEEM III microscope (Elmitec GmbH) at the Nanospectroscopy beamline [64] at the Elettra synchrotron in Basovizza, Trieste, Italy and at the CIRCE beamline with the collaboration of ALBA staff [65]. To fit the linescan of Fig. 1(b), the standard deviation of the spatial Gaussian convolution σ is used as a free parameter [53] leading to $2\sigma = 40$ nm. In Fig 3(b), σ is deduced from a fit with an error function of a linescan of the topological image of the dot, which leads to $2\sigma = 28$ nm.

Brillouin light scattering experiment The Brillouin light scattering experiments setup and conditions are the same as described in Ref. [43]. A backscattering geometry has been used. The investigated spin wave vector lies in the plane of incidence and its length is $k_x = 4\pi \sin(\theta_{inc})/\lambda$ (with θ_{inc} the angle of incidence and $\lambda = 532$ nm the wavelength of the illuminating laser). The external magnetic field was applied perpendicular to the incidence plane, which allows spin waves propagating along the in-plane direction perpendicular to the applied field to be probed (Damon-Eshbach geometry).

Micromagnetic simulations The micromagnetic simulations were carried out using different micromagnetic codes: a homemade code [66], the Mumax3 code [67], the OOMMF code [68]. The following parameters were used [53] : $K = 1.45 \times 10^6$ J/m³, $M_s = 1.4 \times 10^6$ A/m, $A = 27.5$ pJ/m, $D = 2.05$ mJ/m² and a film thickness $t = 1.06$ nm. The lateral size of the elementary cells was typically between 1 and 3 nm. The results presented in this paper were obtained for a lateral cell size of 1 nm. In Fig. 4(b), a spatial Gaussian convolution with standard deviation $\sigma = 14$ nm was used to simulate the finite lateral spatial resolution of the microscope.

Numerical calculations of the skyrmion energy $E_\sigma(d)$ was calculated numerically by minimizing E_σ with respect to Δ at fixed d . $E_{mag}(d)$ was then evaluated from the total magnetostatic energy E_{mag0} of a Bloch DW in a dot using Ref. [62].

$$E_{mag}(d) = E_{mag0} - t(1 - N_{DW}) \frac{\mu_0 M_s^2}{2} \int_0^R \cos^2 \theta \ 2\pi r dr \text{ with}$$

$$E_{mag0} = \frac{4\pi t}{R} \int_0^\infty [1 - \exp(-\beta x)] I^2(x) dx$$

$$I(x) = \int_0^1 dr' r' J_0(xr') \cos \theta(r')$$

where $r' = r/R$ and J_0 is the Bessel function of order zero. R is the dot radius. $N_{DW} = 0.0188$ was deduced from the width of the DW predicted by the micromagnetic simulations.

Competing Interests The authors declare that they have no competing financial interests.

Acknowledgements The authors would like to thank André Thiaville, Murat Cubukcu, Lorenzo Camosi, Michael Caminale and W. Savero-Torres for discussions and their help in experiments. For their contribution to the CIRCE beamline at the Alba synchrotron, we would like to thank C. Escudero, V. Perez-Dieste, E. Pellegrin, J. Nicolas and S. Ferrer. S.P. and J.V. acknowledge the support of the Agence Nationale de la Recherche, project ANR-14-CE26-0012 (ULTRASKY).

Author Contributions O.B. conceived and designed the experiments. O.B., J.V., S.P., D.S.C., A.L, T.O.M., A.S., L.A., M.F. participated in the XMCD-PEEM experiments. O.B and J.V. analyzed the microscopy data. H.Y. and M.C. carried out the *ab-initio* calculations. O.B., L.B-D. and O.K. carried out the micromagnetic simulations, O.B. carried out the numerical calculations, S.A. deposited the magnetic multilayers, M.B., Y.R., A.S. carried out the BLS experiments. O.B. wrote the manuscript. All authors discussed the results and commented on the manuscript.

Correspondence Correspondence and requests for materials should be addressed to O.B. (email: olivier.boule@cea.fr).